Book Chapter

Identification of IDH-Mutation in Grade-4 Astrocytomas using Conventional MRI Derived Radiomic Features

Seyyed Ali Hosseini[1,2]*, Elahe Hosseini[3], Ghasem Hajianfar[4], Isaac Shiri[5], Stijn Servaes[1,2], Pedro Rosa-Neto[1,2], Laiz Godoy[6], MacLean P Nasrallah[7], Donald M O'Rourke[8], Suyash Mohan[6] and Sanjeev Chawla[6]*

[1]Translational Neuroimaging Laboratory, The McGill University Research Centre for Studies in Aging, Douglas Hospital, McGill University, Canada
[2]Department of Neurology and Neurosurgery, Faculty of Medicine, McGill University, Canada
[3]Department of Electrical and Computer Engineering, Kharazmi University, Iran
[4]Rajaie Cardiovascular Medical and Research Center, Iran University of Medical Science, Iran
[5]Division of Nuclear Medicine and Molecular Imaging, Geneva University Hospital, Switzerland
[6]Department of Radiology, Perelman School of Medicine at the University of Pennsylvania, USA
[7]Department of Pathology and Laboratory Medicine, Perelman School of Medicine, University of Pennsylvania, USA
[8]Department of Neurosurgery, Perelman School of Medicine, University of Pennsylvania, USA

***Corresponding Authors:** Seyyed Ali Hosseini, Translational Neuroimaging Laboratory, The McGill University Research Centre for Studies in Aging, Douglas Hospital, McGill University, Montréal, QC H4H 1R3, Canada

Sanjeev Chawla, Department of Radiology, Perelman School of Medicine at the University of Pennsylvania, Philadelphia, PA 19104, USA

Published **June 02, 2023**

This Book Chapter is a republication of an article published by Sanjeev Chawla, et al. at Cancers in February 2023. (Hosseini, S.A.; Hosseini, E.; Hajianfar, G.; Shiri, I.; Servaes, S.; Rosa-Neto, P.; Godoy, L.; Nasrallah, M.P.; O'Rourke, D.M.; Mohan, S.; Chawla, S. MRI-Based Radiomics Combined with Deep Learning for Distinguishing IDH-Mutant WHO Grade 4 Astrocytomas from IDH-Wild-Type Glioblastomas. Cancers 2023, 15, 951. https://doi.org/10.3390/cancers15030951)

How to cite this book chapter: Seyyed Ali Hosseini, Elahe Hosseini, Ghasem Hajianfar, Isaac Shiri, Stijn Servaes, Pedro Rosa-Neto, Laiz Godoy, MacLean P Nasrallah, Donald M O'Rourke, Suyash Mohan, Sanjeev Chawla. Identification of IDH-Mutation in Grade-4 Astrocytomas using Conventional MRI Derived Radiomic Features. In: Prime Archives in Cancer Research: 3rd Edition. Hyderabad, India: Vide Leaf. 2023.

Author Contributions: For research articles with several authors, a short paragraph specifying their individual contributions must be provided. The following statements should be used "Conceptualization, SC, and SAH.; methodology, SC, SAH, LG, MPN, DMP, SM; software, SAH, EH, GH, IS, PR.; validation, SC, SAH, EH, GH and IS, PR; SAH; investigation, SAH, LG; resources, SC; data curation, SAH, LG.; writing—SC, SAH; writing—review and editing, SC, SAH, LG, MPN, DMP, SM, EH, GH, IS, PR; visualization, SAH; supervision, SC; project administration, SC and SAH.; funding acquisition, SC. All authors have read and agreed to the published version of the manuscript."

Funding: "This work was partially supported by a grant obtained from Research Foundation of University of Pennsylvania, Philadelphia, PA, USA (PI= SC)".

Institutional Review Board Statement: This study was approved by the institutional review board (protocol # 829645) and was compliant with the health insurance portability and accountability act (HIPPA).

Informed Consent Statement: "Informed consent was obtained from all subjects involved in the study."

Data Availability Statement: The data supporting this study's findings and data processing algorithms will be available from the investigative team upon reasonable request.

Acknowledgments: We thank Ms. Lisa Desiderio, Senior Research Manager, University of Pennsylvania neuroradiology clinical research division, and MRI technicians for their valuable contributions to this project.

Conflicts of Interest: The authors have no conflicts to disclose.

Introduction

Glioblastomas (GBMs) are devastating and universally fatal brain cancers in adults despite advancements in diagnostic and therapeutic strategies [1]. Approximately 14,000 new cases of GBM are diagnosed in the USA each year, with an estimated incidence of 3.19 per 100,000 people [2]. In recent years, the emergence of molecular profiling in neuro-oncology has had a considerable bearing on the classification, diagnosis, prognosis, and clinical management of GBM patients [3].

The 2016 WHO classification system recognized the somatic mutation of the isocitrate dehydrogenase (IDH) gene in gliomas as a distinct entity regardless of histopathological features [4]. IDH mutation occurs in 50-70% of WHO grade-2/3 gliomas and 10% of GBMs [5], which has been considered a new paradigm in determining the prognosis of these patients. The new 2021 WHO system has reclassified GBMs as IDH mutant grade-4 astrocytomas or IDH wild-type GBMs based on gene expression profiles [6]. It has been widely reported that glioma patients harboring IDH mutations demonstrate a better response to

chemoradiation therapy and live longer than those with IDH wild-type alleles [7,8]. Although, at the same time, immunohistochemical analyses and exomic sequencing are considered gold standards for determining IDH mutation status in gliomas [9,10], tissue heterogeneity, partial sampling of tissue specimens, and presence of variable amounts of antigens constraint the utility of these methods in reliable detection of IDH mutation status [11]. Moreover, it is not always possible to perform neurosurgical interventions because of the eloquent locations of these neoplasms.

Therefore, non-invasive identification of IDH mutant gliomas is vital for making informed decisions on therapeutic intervention and prognosticating these patients. Evidence supports that cancer-associated IDH mutations block normal cellular differentiation and promote tumorigenesis via the abnormal production of 2-hydroxyglutarate (2-HG), a potential oncometabolite [12]. Structurally, the oncometabolite 2HG consists of a 5-spin system and the scalar (J) coupling pattern of 2HG leads to several multiplets with spectral peaks centered around 4.02 (H2), 1.9 (H3 and H3′), and 2.25 ppm (H4 and H4′) spectral locations. The noninvasive detection of 2HG on conventional proton MR Spectroscopy (1H-MRS) is challenging due to the extensive overlap of its resonances with those from metabolites, namely, NAA, glutamate (Glu), glutamine (Gln), gamma-aminobutyric acid (GABA), and lipids. Some prior studies [13-15] have employed sophisticated 1H-MRS acquisition and postprocessing strategies for reliable in-vivo detection and quantification of 2HG. However, not all IDH-mutant gliomas show the neomorphic activity of the 2-HG production [16]. Moreover, these sophisticated ^{1}H-MRS sequences are not readily available in routine clinical settings.

Conventional magnetic resonance imaging (MRI) remains the mainstay for determining tumor location, size, and structural features in neurooncology [17]. Radiomics is a rapidly evolving translational field that automatically produces mineable high-dimensionality data from positron emission tomography (PET), computed tomography (CT), and MRI images with high precision [18-25]. Several previous studies have documented the

clinical potential of quantitative radiomic features extracted from conventional MRI data in diagnosis, determining molecular signatures, assessing treatment response, and predicting survival outcomes in GBM patients [26-30]. Some other studies have also reported promising findings in identifying IDH mutant grade-4 astrocytomas using conventional neuroimaging-based radiomic classification models with variable accuracies [31,32]. However, these studies were limited by the extraction of a sparse number of radiomic features (n=31) [31] or by the inclusion of a small sample size of IDH mutant grade-4 astrocytomas (n=7) [32].

With these inadequacies in mind, the current study was designed to investigate the potential of radiomic features extracted from different tumor habitats as visible on widely available. Therefore, it universally acquired preoperative post-contrast T1 weighted and T2-FLAIR images in differentiating IDH-mutant grade-4 astrocytomas from IDH wild-type GBMs.

Materials and Methods

Patient Population

This retrospective study was approved by the institutional review board and was compliant with the Health Insurance Portability and Accountability Act. The inclusion criteria for enrollment in the present study were that all patients had (a) histopathologically confirmed grade-4 astrocytoma according to the WHO classification system, (b) known IDH mutation genotype using immunohistochemistry and/or gene sequencing, (c) available preoperative anatomical MR images acquired using identical data acquisition protocol. Based upon the inclusion criteria, a cohort of 57 patients (mean age = 57.7 ± 6.9 years, 39 males and 18 females) with newly diagnosed grade-4 astrocytoma and GBM were recruited in this study. Of these 57 patients, 23 had the IDH-mutant genotype, and 34 had the IDH-wild-type genotype.

Determination of IDH Mutational Status by Immunohistochemistry and Sequencing

Hematoxylin, eosin staining, and immunohistochemistry were conducted on 5-micron thick formalin-fixed (10%) paraffin-embedded tissue sections mounted on Leica Surgipath slides followed by drying for 60 min at 70°C temperature. In addition, immunohistochemistry to detect the IDH1 p.R132H variant was performed by using an anti-IDH1-R132H antibody (Monoclonal Mouse Anti-human IDH1 (R132H), Dianova, DIA Clone H09) and DAB chromogen was performed on a Leica Bond III instrument using Bond Polymer Refine Detection System (Leica Microsystems AR9800) following a 20-min heat-induced epitope retrieval with Epitope Retrieval 2, EDTA, pH 9.0. Appropriate positive and negative controls were included.

In addition, massively parallel sequencing or RealTime polymerase chain reaction (PCR) was performed to confirm the immunohistochemical results and to interrogate other IDH variants. For RealTime PCR, formalin-fixed paraffin-embedded (FFPE) specimens with >20% tumor content were analyzed for IDH1 and IDH2 variants using Abbott RealTime Assays (Abbott Molecular, Inc., Abbott Park, IL) after extraction using the QIAamp DSP DNA FFPE Tissue Kit (Qiagen, Hilden, Germany). The Abbott RealTime IDH1 assay detects five single nucleotide variants (SNVs) in IDH1 (p.R132C, p.R132H, p.R132G, p.R132S, and p.R132L). The Abbott RealTime IDH2 assay detects nine SNVs in IDH2 (p.R140Q, p.R140L, p.R140G, p.R140W, p.R172K, p.R172M, p.R172G, p.R172S, and p.R172W). The Abbott m2000rt software performs variant calling, and results are qualitatively reported as positive or not detected. Tests were performed according to the manufacturer's instructions by adding a dilution step to the IDH2 assay. For massively parallel sequencing, the panel gives full gene coverage of 152 genes, using the Agilent Haloplex design with unique molecular identifiers as described previously [33]. Briefly, DNA was extracted from FFPE or specimens preserved in PreservCyt. Samples were multiplexed and sequenced on a HiSeq with total deduplicated reads of 6.5 million/sample; duplicate reads were removed based on incorporating unique molecular identifiers.

All variants were identified using an in-house data processing bioinformatics pipeline capable of detecting SNVs, insertions and/or deletions (indels), and copy number gains for a subset of genes based on increased read depth. An experienced neuropathologist (MPN) reviewed cases from all patients to confirm the IDH status.

MRI Data Acquisition

All Patients underwent MRI on a 3T Tim Trio whole-body MR scanner (Siemens, Erlangen, Germany) equipped with a 12-channel phased array head coil. The anatomical imaging protocol included an axial 3D-T1-weighted magnetization-prepared rapid acquisition of gradient echo (MPRAGE) imaging [repetition time (TR)/echo time (TE)/inversion time (TI)=1760/3.1/950ms]; in-plane resolution=1x1mm^2; slice thickness=1mm; the number of slices=192; and axial T2-FLAIR imaging (TR/TE/TI = 9420/141/2500ms, slice thickness=3mm; the number of slices=60). The postcontrast T1-weighted images were acquired with the same parameters as the precontrast acquisition after administration of the standard dose of gadobenate dimeglumine (MultiHance, Bracco Imaging, Milano, Italy) intravenous contrast agent using a power injector (Medrad, Idianola, PA).

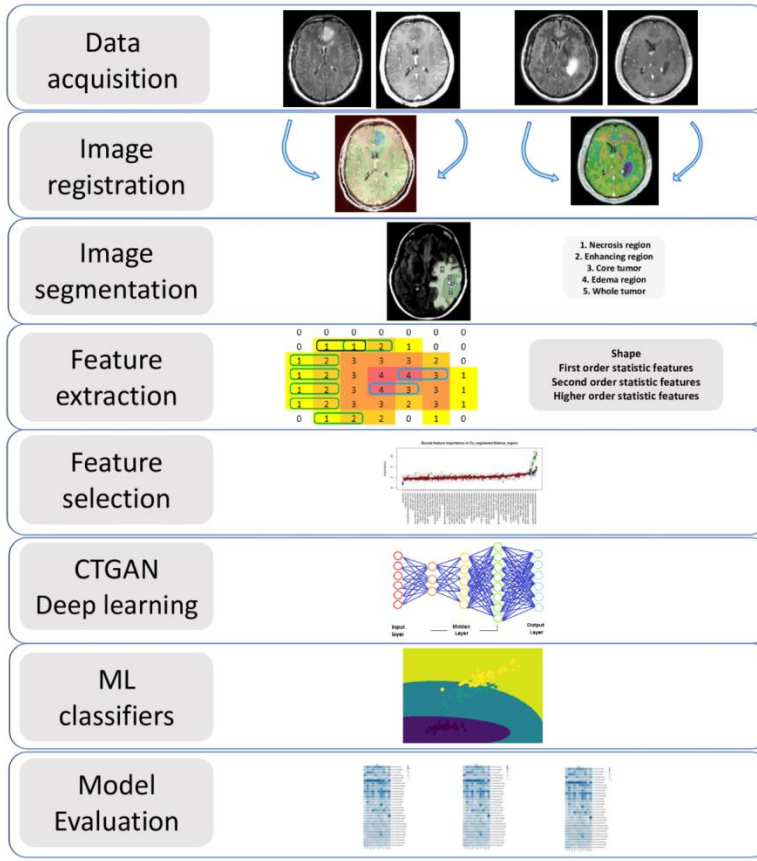

Figure 1: The overview of the image processing pipeline.

Image Processing

The overview of the image processing pipeline, which included image registration, tissue segmentation, feature extraction, feature selection, and radiomics model building, is shown in Figure 1. An investigator (SAH) blinded to the IDH mutational status performed all the image processing steps. Post-contrast T1-weighted images were resliced, resampled, and co-registered with T2-FLAIR images using a linear affine transformation. A semi-automatically segmentation approach was used to generate regions of interest (ROIs) on the anatomical images. Care was

taken to exclude surrounding normal brain vessels. Manual inspections were performed by an experienced neuroradiologist to correct for any pixel anomalies present within the ROIs. Accordingly, these ROIs were modified manually by adding pixels for tumor regions not included in the initial ROIs or by removing pixels for non-tumor regions included in the initial ROIs. Post-contrast T1 weighted images were used to segment solid/contrast-enhancing regions, necrotic regions, and core tumors (solid + necrotic region). T2-FLAIR images were used to segment peri-tumoral edematous regions and whole tumor volumes. All the segmentations were performed using MATLAB 2022a. To maximize the characterization of tumors, these 5 segmented ROIs were overlaid on the source post-contrast T1 weighted images and T2-FLAIR images for the data analysis (Figures 2 and 3). A bias field correction using N4 and an image normalization using histogram matching were performed using the 3D Slicer software on the MRI images before feature extraction to avoid any potential bias field distortions and data heterogeneity bias.

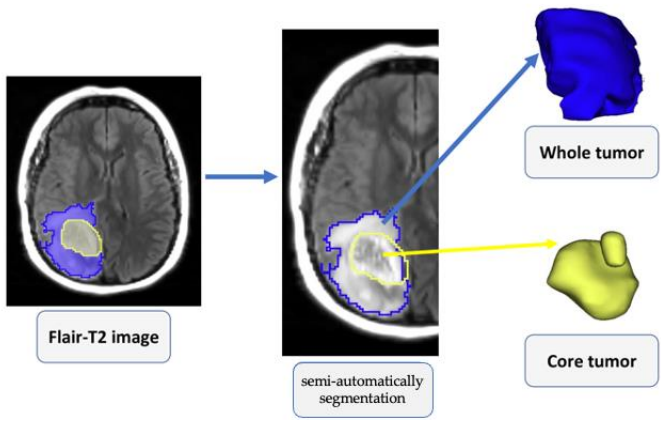

Figure 2: 2D and 3D visualization of various sub-regions of a grade-4 astrocytoma as visible on post-contrast T1 weighted image.

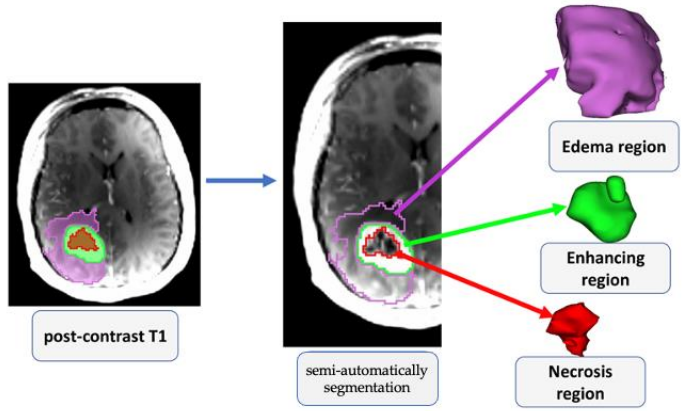

Figure 3: 2D and 3D visualization of various sub-regions of a grade-4 astrocytoma as visible on T2-FLAIR image.

Radiomic Feature Extraction

From each segmented ROI, 105 original radiomic features from categories (shape, first-order statistical, and second-order texture, and higher-order statistic) were extracted using the PyRadiomics package in python [34]. These original features can be sub-divided into 7 classes, including 13 shape features, 18 first-order statistical features, 23 gray level co-occurrence matrix (GLCM) features, 14 gray level dependence matrix (GLDM) features, 16 gray level size zone matrix (GLSZM) features, 16 gray level run length matrix (GLRLM) features, and 5 neighboring gray-tone difference matrix (NGTDM) features. Altogether, 525 radiomic features were extracted from 5 ROIs of each image for a total of 1050 features from post-contrast T1 and T2-FLAIR images. The features comply with feature definitions described by the Imaging Biomarker Standardization Initiative (IBSI) [35]. A high-performance computer system with 16GB RAM and an Intel Core i7-7700 CPU processor @3.60 GHz was used for our data processing. The feature extraction took an average of 2-3 minutes per patient image set. A list of all features is summarized in Supplementary Table S1.

Radiomics Feature Selection

Because radiomics has a highly redundant feature space, it is imperative to reduce the number of correlated features to avoid collinearity. Multiple feature selection algorithms were employed to select image features, including recursive feature elimination (RFE), minimum redundancy, maximum relevance (mRmR), and K-best. Patients were divided into two mutually exclusive training (80%, 50%, and 30%) and testing (20%, 50%, and 70%) sets using the random shuffling method. On training data, Z-score normalization was performed, and the mean and standard deviation of training data were applied to testing data sets. The mRmR feature selection technique was used to select 15 features.

Deep Learning Approach for Data Augmentation

The current study implemented a deep learning method based on generative adversarial networks (GAN) for data augmentation [36]. CTGAN is a GAN-based deep learning data synthesizer to increase the number of our data sets that can improve the reproducibility and discriminatory power of radiomics features [37-39]. After splitting the data set and selecting bold features using various feature selection algorithms, the selected radiomic features from each model with the highest number were used as the input value for CTGAN to synthesize 200 radiomic features. As a result, after splitting 80%, 50%, and 30% of 57 original data for the training sets, 245, 228, and 217 data sets (80%, 50%, and 30% of 57 + 200= 245, 228, and 217) including original and generated data were synthesized, respectively. Different splitting percentages were used to validate our findings [40] and to prevent the impact of data leakage on our results [41]. Furthermore, a random noise (normal distribution, mean=0.0, standard deviation=0.05) [42] was added to the training set. The test sets were not generated, and the original data sets were used for the testing sets.

Machine Learning Classifiers for Prediction Model Building

To develop a prediction model for distinguishing IDH mutant grade-4 astrocytomas from IDH wild-type GBMs, a total of 18 single and ensembled machine learning classifiers [Bernoulli Naïve Bayes (BNB), Multilayer Perceptron(MLP), Support Vector Classifier (SVC), Gaussian Naïve Bayes (GNB), Quadratic Discriminant Analysis (QDA), Bagging Classifier, Linear Discriminant Analysis (LDA), Logistic Regression (RG), Ridge, Ada Boost (AD), Hist Gradient Boosting (HGB), K-Neighbors (KN) (K=5), Random Forest (RF), Gradient Boosting (GB), Extra Trees (ET), Decision Tree (DT), Nearest Centroid (NC), and Passive Aggressive (PA] were employed using an in-house developed python package. All cases in the training cohort (80%, 50%, and 30%) were used to train the classifiers, and and internal validation (cross-validation) was performed from the testing cohort (20%, 50%, and 70%). Receiver operative characteristic (ROC) curve analyses were performed to evaluate the diagnostic potentials of prediction models in distinguishing two groups (IDH-mutant grade-4 astrocytomas and IDH wild-type GBMs). Area under the ROC curve (AUC), area under the precision-recall curve (PR_AUC), accuracy (ACC), sensitivity, specificity, and negative and positive predictive values (NPV and PPV, respectively) were determined for each prediction model as performance metrics.

Results

When original MRI data (n=57) were used in discriminating IDH-mutant grade-4 astrocytomas from IDH wild-type GBMs, the best discriminatory performance (AUC=0.93, ACC=0.92, sensitivity=1, specificity=0.86, PR_AUC=0.92) was obtained from solid/contrast enhancing, and core tumor (solid + necrotic region) overlaid on post-contrast T1 weighted images using various combinations of feature selection algorithms and machine learning classifiers. The predictive power, accuracy, sensitivity, specificity, and PR_AUC of the best 10 methods in distinguishing two genotypes of grade-4 astrocytomas are summarized in Table 1.

Table 1: Best ten performances of multi-machine learning algorithms, feature selection, and multi-segmentation approaches in discriminating IDH-mutant grade-4 astrocytomas from IDH wild-type GBMs using original (Or) data set.

Radiomic Feature Combination	AUC	Accuracy	Sensitivity	Specificity	PR_AUC
Or_PC_T1_Core_AB_Kbest	0.93	0.92	1	0.86	0.92
Or_PC_T1_Core_KN_Kbest	0.93	0.92	1	0.86	0.92
Or_PC_T1_Core_LR_Kbest	0.93	0.92	1	0.86	0.92
Or_PC_T1_Core_MLP_Kbest	0.93	0.92	1	0.86	0.92
Or_T2-FLAIR_Enhancing_DT_Kbest	0.93	0.92	1	0.86	0.92
Or_T2-FLAIR _Enhancing_DT_mRmR	0.93	0.92	1	0.86	0.92
Or_T2-FLAIR _Enhancing_GB_mRmR	0.93	0.92	1	0.86	0.92
Or_T2-FLAIR _Enhancing_RF_mRmR	0.93	0.92	1	0.86	0.92
Or_PC_T1_ Enhancing_HGB_RFE	0.93	0.92	1	0.86	0.92
Or_PC_T1_ Enhancing_HGB_mRmR	0.93	0.92	1	0.86	0.92

The relative importance of the best 10 methods in terms of predictive power, accuracy, sensitivity, specificity, and PR_AUC in discriminating two genotypes of grade-4 astrocytomas by using various combinations of feature selection algorithms, machine learning classifiers, and segmented image regions from 80%, 50%, and 30% of the generated data as training sets are summarized in Tables 2, 3, and 4, respectively. From generated data using 80% training set (Table 2), core regions overlaid on post-contrast T1 images with Kbest and RFE feature selection and GNB and PA classifier and enhancing regions overlaid on T2-FLAIR images with Kbset feature selection and DT and Bagging classifier provided the best discriminatory power (AUC=0.93, accuracy =0.92, sensitivity =1, specificity =0.86, and PR_AUC= 0.92) in distinguishing two genotypes of grade-4 astrocytomas. From generated data using a 50% training set (Table 3), necrosis regions of co-registered post-contrast T1 image with mRmR feature selection and Bagging and RF classifier and edematous core of co-registered post-contrast T1 image with Kbest feature selection and KN classifier provided the highest predictive power (AUC=0.92, accuracy =0.92, sensitivity =0.91, specificity =0.94, and PR_AUC=0.93). From generated data using a 30% training set (Table 4), the core regions of co-registered post-contrast T1 image with K-best feature selection and LR classifier provided the highest predictive power (AUC=0.91, accuracy =0.92, sensitivity =0.86, specificity =0.96, and PR_AUC=0.92).

Table 2: Best ten performances of multi-machine learning algorithms, feature selection, and multi-segmentation approach in discriminating IDH-mutant grade-4 astrocytomas from IDH wild-type GBMs using generated (Ge) data with 80% training set.

Radiomic Feature Combination	AUC	Accuracy	Sensitivity	Specificity	PR_AUC
Ge_PC_T1_Core_GNB_Kbest	0.93	0.92	1	0.86	0.92
Ge_PC_T1_Core_PA_RFE	0.93	0.92	1	0.86	0.92
Ge_T2_FLAIR_Enhancing_Bagging_Kbest	0.93	0.92	1	0.86	0.92
Ge_T2_FLAIR_Enhancing _DT_Kbest	0.93	0.92	1	0.86	0.92
Ge_T2_FLAIR_Whole _AB_Kbest	0.90	0.92	0.80	1	0.94
Ge_PC_T1_Core_RF_Kbest	0.90	0.92	0.80	1	0.94
Ge_PC_T1_Core_RF_RFE	0.90	0.92	0.80	1	0.94
Ge_PC_T1_Core_HGB_Kbest	0.90	0.92	0.80	1	0.94
Ge_PC_T1_Edema_AB_Kbest	0.90	0.92	0.80	1	0.94
Ge_PC_T1_Edema_Bagging_Kbest	0.90	0.92	0.80	1	0.94

Table 3: Best ten performances of multi-machine learning algorithms, feature selection, and multi-segmentation approach in discriminating IDH-mutant grade-4 astrocytomas from IDH wild-type GBMs using generated (Ge) data with 50% training set.

Radiomic Feature Combination	AUC	Accuracy	Sensitivity	Specificity	PR_AUC
Ge_PC_T1_ Necrosis_Bagging_mRmR	0.92	0.92	0.91	0.94	0.93
Ge_PC_T1_ Necrosis_RF_mRmR	0.92	0.92	0.91	0.94	0.93
Ge_PC_T1_ Edema_KN_mRmR	0.92	0.92	0.91	0.94	0.93
Ge_PC_T1_ Necrosis_KN_RFE	0.89	0.89	0.91	0.87	0.89
Ge_PC_T1_ Edema_HGB_RFE	0.89	0.89	0.91	0.87	0.89
Ge_PC_T1_ Necrosis_KN_RFE	0.88	0.89	0.82	0.94	0.90
Ge_PC_T1_ Necrosis_KN_RFE	0.88	0.89	0.82	0.94	0.90
Ge_PC_T1_ Edema_HGB_RFE	0.88	0.89	0.82	0.94	0.90
Ge_PC_T1_ Edema_HGB_RFE	0.88	0.89	0.82	0.94	0.90
Ge_PC_T1_ Core_KN_RFE	0.88	0.89	0.82	0.94	0.90

Table 4: Best ten performances of multi-machine learning algorithms, feature selection, and multi-segmentation approach in discriminating IDH-mutant grade-4 astrocytomas from IDH wild-type GBMs using generated (Ge) data with 30% training set.

Radiomic Feature Combination	AUC	Accuracy	Sensitivity	Specificity	PR_AUC
Ge_PC_T1_ Core_LR_Kbest	0.91	0.92	0.86	0.96	0.92
Ge_PC_T1_ Core_Ridge_Kbest	0.89	0.89	0.86	0.92	0.88
Ge_PC_T1_ Core_SVC_mRmR	0.86	0.89	0.71	1	0.91
Ge_PC_T1_ Core_LDA_Kbest	0.84	0.84	0.86	0.83	0.83
Ge_T2_FLAIR_Core_HGB_Kbest	0.82	0.79	0.93	0.71	0.80
Ge_T2_FLAIR_Core_LR_Kbest	0.81	0.84	0.71	0.92	0.83
Ge_PC_T1_ Edema_GB_Kbest	0.81	0.84	0.71	0.92	0.83
Ge_T2_FLAIR_Core_LDA_Kbest	0.81	0.81	0.78	0.83	0.80
Ge_T2_FLAIR_Core_Ridge_Kbest	0.81	0.81	0.78	0.83	0.80
Ge_PC_T1_ Enhancing_QDA_Kbest	0.80	0.79	0.86	0.75	0.79

Heatmaps of predictive power (AUC), predictive accuracy (ACC), sensitivity (SEN), and specificity (SPE) for discriminating IDH-mutant grade- 4 astrocytomas from IDH wild-type GBMs utilizing a variety of feature selection (training set equal to 80%), and machine learning algorithms applied to distinct subregions of neoplasms are shown in Figures 4-7 respectively. In addition, the comprehensive findings from multi-machine learning algorithms, feature selection, and multi-segmentation approach in discriminating IDH-mutant grade-4 astrocytomas from IDH wild-type GBMs of original and generated data with different training and testing sets are provided in the supplementary file.

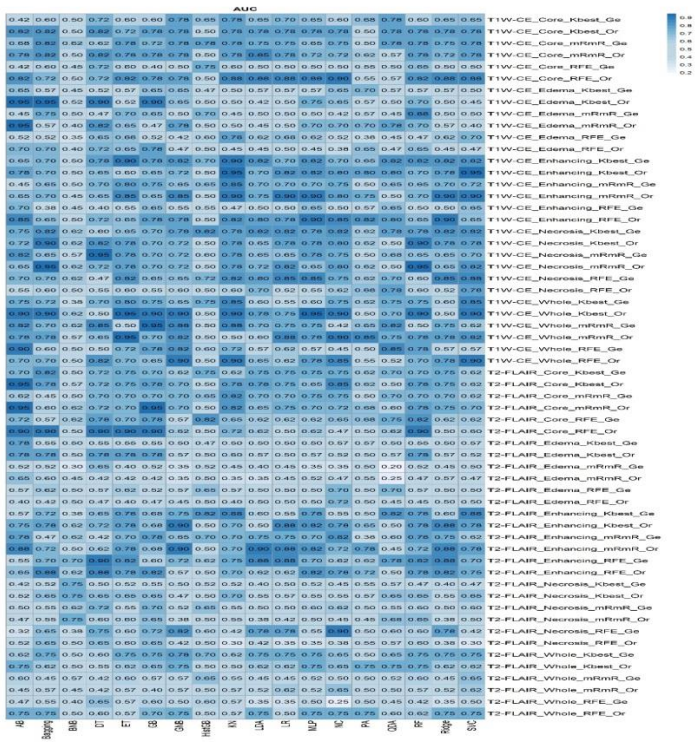

Figure 4: Area under the ROC curve (AUC, predictive power) heatmap using a variety of combinations of anatomical images, tumor habitats, radiomic features and machine learning classifiers in differentiating IDH-mutant grade- 4 astrocytomas from IDH wild-type GBMs.

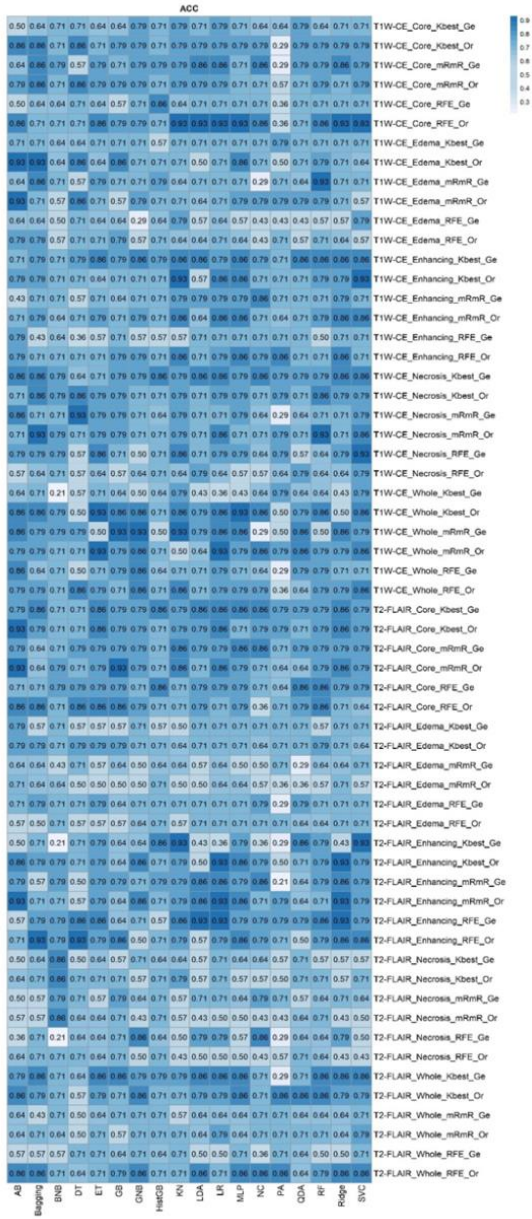

Figure 5: Accuracy (ACC) heatmap using a variety of combinations of anatomical images, tumor habitats, radiomic features and machine learning classifiers in differentiating IDH-mutant grade- 4 astrocytomas from IDH wild-type GBMs.

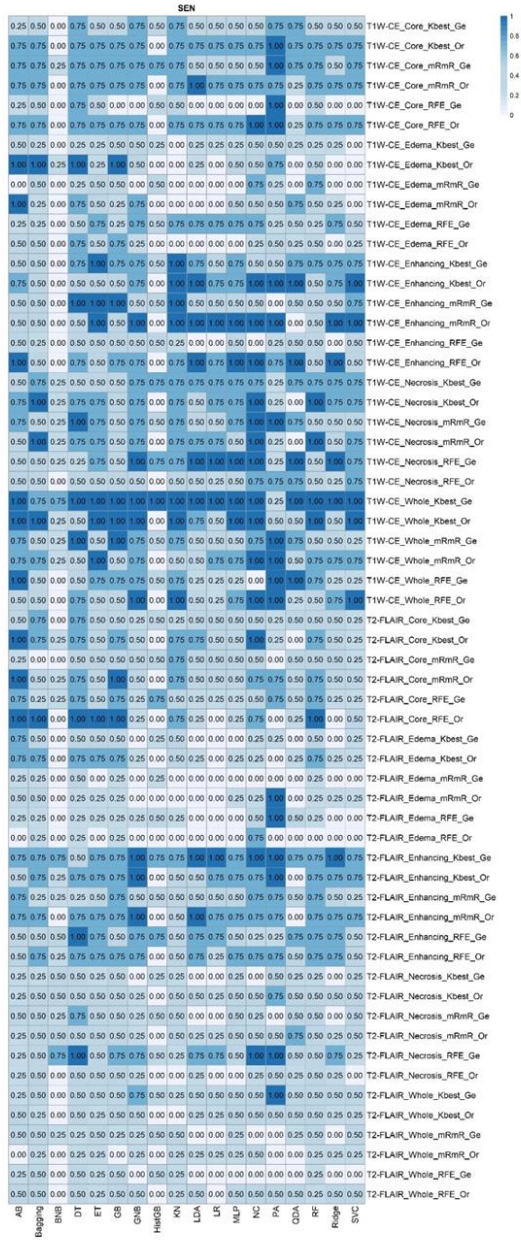

Figure 6: Sensitivity heatmap using a variety of combinations of anatomical images, tumor habitats, radiomic features and machine learning classifiers in differentiating IDH-mutant grade- 4 astrocytomas from IDH wild-type GBMs.

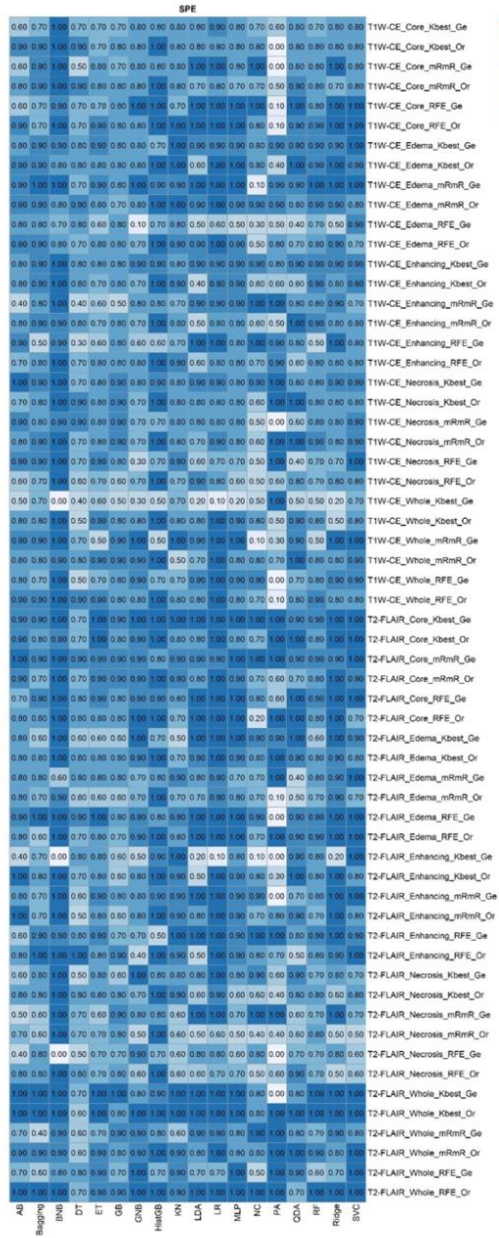

Figure 7: Specificity heatmap using a variety of combinations of anatomical images, tumor habitats, radiomic features and machine learning classifiers in differentiating IDH-mutant grade- 4 astrocytomas from IDH wild-type GBMs.

Discussion

In this study, we investigated the clinical utility of a conventional neuroimaging-based radiomics approach with deep learning in determining the IDH status of astrocytomas. A total of 1050 radiomic features were extracted from different tumor habitats (solid/contrast enhancing, central necrotic, peritumoral edematous, core tumor, and whole tumor regions), encompassing post-contrast T1 weighted and T2-FLAIR images. Our work is an extension of previous studies as we used GAN based algorithm to increase our sample size and a large number of machine learning classifiers (n=18) to build a reliable prediction model in distinguishing IDH mutant grade-4 astrocytomas and IDH wild-type GBMs. In the validating cohort, our best prediction model consisted of central necrotic region and whole tumor volumes from post-contrast T1 weighted images when a combination of mRmR radiomic feature extraction algorithm and GB machine learning classifier were used together. This prediction model achieved a high diagnostic performance (AUC=0.93, accuracy=0.92, sensitivity=1, specificity=0.86, PR_AUC=0.92) in discriminating two genotypes of grade-4 astrocytomas.

IDH mutation has been recognized as one of the most important molecular markers for diagnosing gliomas and GBMs based on the 2016 WHO classification [4]. In addition, according to the recent 2021 WHO classification of tumors of the central nervous system (CNS) [6], previously called IDH mutant, GBM is now designated as IDH-mutant grade-4 astrocytoma, and GBM is diagnosed in the setting of IDH wild-type status. It has been reported that IDH mutational status is an independent favorable prognostic factor for conferring longer progression-free and overall survivals in GBM patients [7,8]. Moreover, patients with IDH mutant grade-4 gliomas have been shown to exhibit a better prognosis than those with IDH wild-type grade-3 gliomas. Collectively, these clinical findings emphasize the importance of determining IDH mutant status in grade-4 astrocytomas [43]. The immunohistochemical assay is the most commonly used method for assessing IDH mutation status following invasive surgical interventions, which are associated with operative risks

[44,45]. Moreover, the possibility of sampling error is highly relevant to determining histological grade [46] and molecular profiling [11,46]. For example, IDH sequencing may be falsely negative if there are few glioma cells present within a tumor specimen [46] or substantial genetic heterogeneity occurs within the tumor specimen [11]. In addition, some exome sequencing studies have reported that traditional immunohistochemical assays do not detect IDH mutant status in ~15% of gliomas [47]. Therefore, it is essential to develop non-invasive and objective imaging biomarkers for identifying IDH mutant status in gliomas.

Mechanistically, wild-type IDH normally catalyzes the reversible, NADP+-dependent oxidative decarboxylation of isocitrate to alpha-ketoglutarate (α-KG) in the TCA cycle. However, IDH mutations confer a neomorphic enzyme activity converting α-KG to 2HG. Therefore, the oncometabolite 2HG has been proposed as a putative biomarker for IDH-specific genetic profiles for gliomas. A few studies have employed sophisticated spectroscopic sequences and post-processing tools for detecting spectral resonances of 2HG from IDH mutant gliomas [15,48-50]. However, the non-availability of these sequences and tools in routine clinical settings renders these techniques less attractive. Moreover, diagnostic challenges may also arise because of the presence of a high degree of genetic heterogeneity within GBMs and partial sampling of these lesions, especially when single voxel spectroscopic methods are employed. In contrast, conventional MRI is a widely available, fast, easy-to-use, and economically affordable imaging modality that provides valuable information about brain tumor structural and morphological characteristics. Qualitative imaging features such as frontal lobe tumor location, homogeneous signal intensity, sparse contrast enhancement within the tumor beds, and less intensive tumor infiltration are some of the imaging characteristics that have been used to identify IDH mutant gliomas with variable success [51-53]. However, all these qualitative associations were largely based on univariate analyses and hence, were prone to interrater variably. Therefore, a comprehensive analysis of imaging features is warranted for

reliable prediction of IDH mutation status in spatially and temporally heterogeneous GBMs.

Radiomics is a quantitative analytical method of medical images that provides information that is generally difficult to perceive by visual inspection. Compared to conventional analytical approaches, radiomics analysis can provide a more efficient and unbiased quantification of imaging information. Readily interpretable and quantitative features such as intensity distributions, spatial relationships, textural heterogeneity, and shape descriptors are extracted from a pre-defined ROI encompassing both solid and peritumoral regions of neoplasms in a typical fashion [54]. The training cohort is used to instruct the computer algorithm to detect patterns of features that are subsequently examined in a validation cohort to evaluate the algorithm's performance in correctly predicting the presence or absence of a feature and its association with an outcome. In the recent past, the field of radiogenomics has been established to study the relationship between imaging features and underlying molecular processes and characteristics. Recently, it has been widely reported that radiomics/radiogenomics aids in guiding clinical decision-making in neuro-oncology, particularly for making an accurate diagnosis, prognosis, and response assessment [26-30,55].

IDH mutation occurs only in 10% of grade-4 astrocytomas, so we could only include data from 23 IDH mutant cases in the present study. Because of this small sample size and imbalance in data distribution, our data was prone to overfitting. Furthermore, in situations with an insufficient number of training data sets, the model is often overtrained. Consequently, the model performs well during the training stage but comparatively poorly during the subsequent testing stage. To address this challenge of small sample size, we leveraged the use of a well-established GAN method for synthesizing high-quality images and, in turn, raising the total sample size from 57 to 200. GAN is a deep learning architecture in which two neural networks compete against each other in a zero-sum game framework [56]. A GAN model consists of two components: a generator and a discriminator. In the training stage, the data sets produced by the

generator, along with real images, serve as inputs to the discriminator. This can be considered comparable to enlarging the training datasets for the discriminator, whose purpose is to differentiate real from the generated images [57]. Consequently, the discriminator will not immediately succumb to overfitting through the competitive relationship between these two networks, even when a limited number of training samples are used.

In a previous study [58], when a random forest classifier was applied to a mixed population of grade-III and grade-IV gliomas, high accuracies (86-89%) were observed in identifying IDH mutation status. In the present study, only a histologically homogenous population of gliomas (grade-IV astrocytomas) was included. Moreover, numerous radiomics features and machine learning classifiers were applied to predict IDH mutation status. Tumor necrosis was recognized as an important imaging feature and contributed most to the prediction model for distinguishing IDH mutant grade-4 astrocytomas from IDH wild-type GBMs when the Kbest radiomics feature algorithm and decision tree (DT) classifier was used together. This finding is in agreement with an earlier study [58] in which IDH mutation was associated with a smaller enhancing volume and a larger necrotic volume when multiparametric radiomic profiles were analyzed. Additionally, imaging features from whole tumor volumes were found to be associated with IDH mutation status when the Kbest radiomics feature selection algorithm, and AB classifier were used together (AUC= 0.93). This finding may be explained by the fact that IDH mutant gliomas have a more heterogeneous imaging microenvironment because of their stepwise gliomagenesis [59]. Our findings are also consistent with previous studies that have reported a larger tumor volume [60] and a lower degree of cellularity [61] in IDH mutants than in IDH wild-type gliomas. Our results and published findings indicate that quantitative radiomics features can predict the IDH mutation status of grade-4 astrocytomas with high diagnostic power.

Our findings warrant further validation in multicentric, prospective studies with larger patient populations. In

conclusion, a prediction model based on conventional MRI-extracted radiomic features achieved promising diagnostic power in distinguishing IDH mutant grade-4 astrocytomas from IDH wild-type GBMs.

Conclusions

In conclusion, a prediction model based on conventional MRI-extracted radiomic features achieved promising diagnostic power in distinguishing IDH mutant grade-4 astrocytomas from IDH wild-type GBMs.

References

1. Wen PY, Weller M, Lee EQ, Alexander BM, Barnholtz-Sloan JS, et al. Glioblastoma in adults: a Society for Neuro-Oncology (SNO) and European Society of Neuro-Oncology (EANO) consensus review on current management and future directions. Neuro-oncology. 2020; 22: 1073-1113.
2. Alexander BM, Cloughesy TF. Platform trials arrive on time for glioblastoma. Oxford: Oxford University Press US. 2018; 723-725.
3. Thakkar JP, Dolecek TA, Horbinski C, Ostrom QT, Lightner DD, et al. Epidemiologic and Molecular Prognostic Review of GlioblastomaGBM Epidemiology and Biomarkers. Cancer epidemiology, biomarkers & prevention. 2014; 23: 1985-1996.
4. Louis DN, Perry A, Reifenberger G, Von Deimling A, Figarella-Branger D, et al. The 2016 World Health Organization classification of tumors of the central nervous system: a summary. Acta neuropathologica. 2016; 131: 803-820.
5. Vigneswaran K, Neill S, Hadjipanayis CG. Beyond the World Health Organization grading of infiltrating gliomas: advances in the molecular genetics of glioma classification. Annals of translational medicine. 2015; 3.
6. Louis DN, Perry A, Wesseling P, Brat DJ, Cree IA, et al. The 2021 WHO classification of tumors of the central nervous system: a summary. Neuro-oncology. 2021; 23: 1231-1251.
7. Yan W, Zhang W, You G, Bao Z, Wang Y, et al. Correlation

of IDH1 mutation with clinicopathologic factors and prognosis in primary glioblastoma: a report of 118 patients from China. PloS one. 2012; 7: e30339.
8. Zhang CB, Bao ZS, Wang HJ, Yan W, Liu YW, et al. Correlation of IDH1/2 mutation with clinicopathologic factors and prognosis in anaplastic gliomas: a report of 203 patients from China. Journal of cancer research and clinical oncology. 2014; 140: 45-51.
9. Parsons DW, Jones S, Zhang X, Lin JCH, Leary RJ, et al. An integrated genomic analysis of human glioblastoma multiforme. science. 2008; 321: 1807-1812.
10. Yan H, Parsons DW, Jin G, McLendon R, Rasheed BA, et al. IDH1 and IDH2 mutations in gliomas. New England journal of medicine. 2009; 360: 765-773.
11. Preusser M, Wöhrer A, Stary S, Höftberger R, Streubel B, et al. Value and limitations of immunohistochemistry and gene sequencing for detection of the IDH1-R132H mutation in diffuse glioma biopsy specimens. Journal of Neuropathology & Experimental Neurology. 2011; 70: 715-723.
12. Dang L, White DW, Gross S, Bennett BD, Bittinger MA, et al. Cancer-associated IDH1 mutations produce 2-hydroxyglutarate. Nature. 2009; 462: 739-744.
13. Pope WB, Prins RM, Albert Thomas M, Nagarajan R, Yen KE, et al. Non-invasive detection of 2-hydroxyglutarate and other metabolites in IDH1 mutant glioma patients using magnetic resonance spectroscopy. Journal of neuro-oncology. 2012; 107: 197-205.
14. Choi C, Ganji SK, DeBerardinis RJ, Hatanpaa KJ, Rakheja D, et al. 2-hydroxyglutarate detection by magnetic resonance spectroscopy in IDH-mutated patients with gliomas. Nature medicine. 2012; 18: 624-629.
15. Verma G, Mohan S, Nasrallah MP, Brem S, Lee JY, et al. Non-invasive detection of 2-hydroxyglutarate in IDH-mutated gliomas using two-dimensional localized correlation spectroscopy (2D L-COSY) at 7 Tesla. Journal of translational medicine. 2016; 14: 1-8.
16. Ichimura K, Pearson DM, Kocialkowski S, Bäcklund LM, Chan R, et al. IDH1 mutations are present in the majority of common adult gliomas but rare in primary glioblastomas. Neuro-oncology. 2009; 11: 341-347.

17. Villanueva-Meyer JE, Mabray MC, Cha S. Current clinical brain tumor imaging. Neurosurgery. 2017; 81: 397-415.
18. Hosseini SA, Hajianfar G, Shiri I, Zaidi H, editors. Lymphovascular Invasion Prediction in Lung Cancer Using Multi-Segmentation PET Radiomics and Multi-Machine Learning Algorithms. 2021 IEEE Nuclear Science Symposium and Medical Imaging Conference (NSS/MIC). IEEE. 2021.
19. Hosseini SA, Hajianfar G, Shiri I, Zaidi H, editors. Lung Cancer Recurrence Prediction Using Radiomics Features of PET Tumor Sub-Volumes and Multi-Machine Learning Algorithms. 2021 IEEE Nuclear Science Symposium and Medical Imaging Conference (NSS/MIC). IEEE. 2021.
20. Ponsiglione A, Stanzione A, Cuocolo R, Ascione R, Gambardella M, et al. Cardiac CT and MRI radiomics: systematic review of the literature and radiomics quality score assessment. European Radiology. 2021; 1-10.
21. Fathi Kazerooni A, Bagley SJ, Akbari H, Saxena S, Bagheri S, et al. Applications of radiomics and radiogenomics in high-grade gliomas in the era of precision medicine. Cancers. 2021; 13: 5921.
22. Hosseini SA, Shiri I, Hajianfar G, Bagley S, Nasrallah M, et al. MRI based Radiomics for Distinguishing IDH-mutant from IDH wild-type Grade-4 Astrocytomas. Cancers (Basel). 2023; 15: 951.
23. Hosseini SA, Shiri I, Hajianfar G, Bahadorzadeh B, Ghafarian P, et al. Synergistic impact of motion and acquisition/reconstruction parameters on 18F-FDG PET radiomic features in non-small cell lung cancer: Phantom and clinical studies. Medical Physics. 2022; 49: 3783-3796.
24. Hosseini SA, Hajianfar G, Shiri I, Zaidi H, editors. PET Image Radiomics Feature Variability in Lung Cancer: Impact of Image Segmentation. 2021 IEEE Nuclear Science Symposium and Medical Imaging Conference (NSS/MIC). IEEE. 2021.
25. Hosseini SA, Shiri I, Hajianfar G, Ghafarian P, Karam MB, et al. The impact of preprocessing on the PET-CT radiomics features in non-small cell lung cancer. Frontiers in Biomedical Technologies. 2021; 8.
26. Ruan Z, Mei N, Lu Y, Xiong J, Li X, et al. A Comparative

and Summative Study of Radiomics-based Overall Survival Prediction in Glioblastoma Patients. Journal of Computer Assisted Tomography. 2022; 46: 470-479.
27. Aftab K, Aamir FB, Mallick S, Mubarak F, Pope WB, et al. Radiomics for precision medicine in glioblastoma. Journal of neuro-oncology. 2022; 1-15.
28. Baine M, Burr J, Du Q, Zhang C, Liang X, et al. The potential use of radiomics with pre-radiation therapy MR imaging in predicting risk of pseudoprogression in glioblastoma patients. Journal of imaging. 2021; 7: 17.
29. Lu Y, Patel M, Natarajan K, Ughratdar I, Sanghera P, et al. Machine learning-based radiomic, clinical and semantic feature analysis for predicting overall survival and MGMT promoter methylation status in patients with glioblastoma. Magnetic resonance imaging. 2020; 74: 161-170.
30. Sasaki T, Kinoshita M, Fujita K, Fukai J, Hayashi N, et al. Radiomics and MGMT promoter methylation for prognostication of newly diagnosed glioblastoma. Scientific reports. 2019; 9: 1-9.
31. Lee MH, Kim J, Kim ST, Shin HM, You HJ, et al. Prediction of IDH1 mutation status in glioblastoma using machine learning technique based on quantitative radiomic data. World neurosurgery. 2019; 125: e688-e696.
32. Hsieh KLC, Chen CY, Lo CM. Radiomic model for predicting mutations in the isocitrate dehydrogenase gene in glioblastomas. Oncotarget. 2017; 8: 45888.
33. Nasrallah MP, Binder ZA, Oldridge DA, Zhao J, Lieberman DB, et al. Molecular neuropathology in practice: clinical profiling and integrative analysis of molecular alterations in glioblastoma. Academic pathology. 2019; 6: 2374289519848353.
34. Van Griethuysen JJ, Fedorov A, Parmar C, Hosny A, Aucoin N, et al. Computational radiomics system to decode the radiographic phenotype. Cancer research. 2017; 77: e104-e107.
35. Zwanenburg A, Leger S, Vallières M, Löck S. Image biomarker standardisation initiative. arXiv preprint arXiv: 161207003. 2016.
36. Gupta A, Bhatt D, Pandey A. Transitioning from Real to Synthetic data: Quantifying the bias in model. arXiv preprint

arXiv:210504144. 2021.
37. Dina AS, Siddique A, Manivannan D. Effect of Balancing Data Using Synthetic Data on the Performance of Machine Learning Classifiers for Intrusion Detection in Computer Networks. arXiv preprint arXiv:220400144. 2022.
38. Pereira M, Kshirsagar M, Mukherjee S, Dodhia R, Ferres JL. An Analysis of the Deployment of Models Trained on Private Tabular Synthetic Data: Unexpected Surprises. arXiv preprint arXiv:210610241. 2021.
39. Stadler T, Oprisanu B, Troncoso C, editors. Synthetic data–anonymisation groundhog day. 31st USENIX Security Symposium (USENIX Security 22). 2022.
40. Sepehri S, Tankyevych O, Upadhaya T, Visvikis D, Hatt M, et al. Comparison and Fusion of Machine Learning Algorithms for Prospective Validation of PET/CT Radiomic Features Prognostic Value in Stage II-III Non-Small Cell Lung Cancer. Diagnostics. 2021; 11: 675.
41. Hannun A, Guo C, van der Maaten L, editors. Measuring data leakage in machine-learning models with Fisher information. Uncertainty in Artificial Intelligence. PMLR. 2021.
42. Dietterich TG, editor Ensemble methods in machine learning. International workshop on multiple classifier systems. Berlin: Springer. 2000.
43. Hartmann C, Hentschel B, Wick W, Capper D, Felsberg J, et al. Patients with IDH1 wild type anaplastic astrocytomas exhibit worse prognosis than IDH1-mutated glioblastomas, and IDH1 mutation status accounts for the unfavorable prognostic effect of higher age: implications for classification of gliomas. Acta neuropathologica. 2010; 120: 707-718.
44. Bhandari AP, Liong R, Koppen J, Murthy S, Lasocki A. Noninvasive determination of IDH and 1p19q status of lower-grade gliomas using MRI radiomics: a systematic review. American Journal of Neuroradiology. 2021; 42: 94-101.
45. Akay A, Rüksen M, Islekel S. Magnetic resonance imaging-guided stereotactic biopsy: a review of 83 cases with outcomes. Asian Journal of Neurosurgery. 2019; 14: 90.
46. Horbinski C. What do we know about IDH1/2 mutations so

far, and how do we use it? Acta neuropathologica. 2013; 125: 621-636.
47. Gutman DA, Dunn WD, Grossmann P, Cooper LA, Holder CA, et al. Somatic mutations associated with MRI-derived volumetric features in glioblastoma. Neuroradiology. 2015; 57: 1227-1237.
48. Askari P, Dimitrov IE, Ganji SK, Tiwari V, Levy M, et al. Spectral fitting strategy to overcome the overlap between 2-hydroxyglutarate and lipid resonances at 2.25 ppm. Magnetic resonance in medicine. 2021; 86: 1818-1828.
49. Choi C, Raisanen JM, Ganji SK, Zhang S, McNeil SS, et al. Prospective longitudinal analysis of 2-hydroxyglutarate magnetic resonance spectroscopy identifies broad clinical utility for the management of patients with IDH-mutant glioma. Journal of Clinical Oncology. 2016; 34: 4030.
50. An Z, Ganji SK, Tiwari V, Pinho MC, Patel T, et al. Detection of 2-hydroxyglutarate in brain tumors by triple-refocusing MR spectroscopy at 3T in vivo. Magnetic resonance in medicine. 2017; 78: 40-48.
51. Sonoda Y, Shibahara I, Kawaguchi T, Saito R, Kanamori M, et al. Association between molecular alterations and tumor location and MRI characteristics in anaplastic gliomas. Brain tumor pathology. 2015; 32: 99-104.
52. Baldock AL, Yagle K, Born DE, Ahn S, Trister AD, et al. Invasion and proliferation kinetics in enhancing gliomas predict IDH1 mutation status. Neuro-oncology. 2014; 16: 779-786.
53. Qi S, Yu L, Li H, Ou Y, Qiu X, et al. Isocitrate dehydrogenase mutation is associated with tumor location and magnetic resonance imaging characteristics in astrocytic neoplasms. Oncology letters. 2014; 7: 1895-1902.
54. Aerts HJ, Velazquez ER, Leijenaar RT, Parmar C, Grossmann P, et al. Decoding tumour phenotype by noninvasive imaging using a quantitative radiomics approach. Nature communications. 2014; 5: 1-9.
55. Hu S, Luo M, Li Y. Machine Learning for the Prediction of Lymph Nodes Micrometastasis in Patients with Non-Small Cell Lung Cancer: A Comparative Analysis of Two Practical Prediction Models for Gross Target Volume Delineation. Cancer Management and Research. 2021; 13: 4811.

56. Zhu L, Chen Y, Ghamisi P, Benediktsson JA. Generative adversarial networks for hyperspectral image classification. IEEE Transactions on Geoscience and Remote Sensing. 2018; 56: 5046-5063.
57. Creswell A, White T, Dumoulin V, Arulkumaran K, Sengupta B, et al. Generative adversarial networks: An overview. IEEE signal processing magazine. 2018; 35: 53-65.
58. Zhang B, Chang K, Ramkissoon S, Tanguturi S, Bi WL, et al. Multimodal MRI features predict isocitrate dehydrogenase genotype in high-grade gliomas. Neuro-oncology. 2017; 19: 109-117.
59. Lee S, Choi SH, Ryoo I, Yoon TJ, Kim TM, et al. Evaluation of the microenvironmental heterogeneity in high-grade gliomas with IDH1/2 gene mutation using histogram analysis of diffusion-weighted imaging and dynamic-susceptibility contrast perfusion imaging. Journal of neuro-oncology. 2015; 121: 141-150.
60. Metellus P, Coulibaly B, Colin C, de Paula AM, Vasiljevic A, et al. Absence of IDH mutation identifies a novel radiologic and molecular subtype of WHO grade II gliomas with dismal prognosis. Acta neuropathologica. 2010; 120: 719-729.
61. Xing Z, Yang X, She D, Lin Y, Zhang Y, et al. Noninvasive assessment of IDH mutational status in World Health Organization grade II and III astrocytomas using DWI and DSC-PWI combined with conventional MR imaging. American Journal of Neuroradiology. 2017; 38: 1138-1144.

Supplementary Materials

Supplementary Materials can be accessed online at https://videleaf.com/wp-content/uploads/2023/05/PACR3ED-23-05_Supplementary-Materials.pdf